Diffraction-limited integral-field spectroscopy for extreme adaptive optics systems with the multicore fiber-fed integral-field unit

J. of Astronomical Telescopes, Instruments, and Systems, 6(4), 045007 (2020).
https://doi.org/10.1117/1.JATIS.6.4.045007

Diffraction-limited integral-field spectroscopy for extreme adaptive optics systems with the multicore fiber-fed integral-field unit

Sebastiaan Y. Haffert,[a,b,*,†,‡] **Robert J. Harris**,[c,d,†] **Alessio Zanutta**,[e] **Fraser A. Pike**,[f] **Andrea Bianco**,[e] **Eduardo Redaelli**,[e] **Aurélien Benoît**,[f] **David G. MacLachlan**,[f] **Calum A. Ross**,[f] **Itandehui Gris-Sánchez**,[g,h] **Mareike D. Trappen**,[i,j] **Yilin Xu**,[i,j] **Matthias Blaicher**,[i,j] **Pascal Maier**,[i,j] **Giulio Riva**,[e] **Baptiste Sinquin**,[k] **Caroline Kulcsár**,[k] **Nazim Ali Bharmal**,[l] **Eric Gendron**,[m] **Lazar Staykov**,[l] **Tim J. Morris**,[l] **Santiago Barboza**,[d] **Norbert Muench**,[d] **Lisa Bardou**,[l] **Léonard Prengère**,[k] **Henri-François Raynaud**,[k] **Phillip Hottinger**,[c] **Theodoros Anagnos**,[c,n] **James Osborn**,[l] **Christian Koos**,[i,j] **Robert R. Thomson**,[f] **Tim A. Birks**,[g] **Ignas A. G. Snellen**,[a] **and Christoph U. Keller**[a]

[a]Leiden University, Leiden Observatory, RA Leiden, The Netherlands
[b]Unversity of Arizona, Steward Observatory, Tucson, Arizona, United States
[c]Zentrum für Astronomie der Universität Heidelberg, Landessternwarte Königstuhl, Königstuhl, Heidelberg, Germany
[d]Max-Planck-Institute for Astronomy, Königstuhl, Heidelberg, Germany
[e]INAF—Osservatorio Astronomico di Brera, Merate (LC), Italy
[f]Heriot-Watt University, SUPA, Institute of Photonics and Quantum Sciences, Edinburgh, United Kingdom
[g]University of Bath, Department of Physics, Claverton Down, Bath, United Kingdom
[h]Universitat Politècnica de València, ITEAM Research Institute, Valencia, Spain
[i]Institute of Microstructure Technology, Karlsruhe Institute of Technology, Eggenstein-Leopoldshafen, Germany
[j]Institute of Photonics and Quantum Electronics (IPQ), Karlsruhe Institute of Technology (KIT), Karlsruhe, Germany
[k]Université Paris-Saclay, Institut d'Optique Graduate School, CNRS, Laboratoire Charles Fabry, Palaiseau, France
[l]Durham University, Department of Physics, Durham, United Kingdom
[m]Université PSL, CNRS, Sorbonne Université, Université de Paris, LESIA, Observatoire de Paris, Meudon, France
[n]Macquarie University, MQ Photonics Research Centre, Department of Physics and Astronomy, Australia

Abstract. Direct imaging instruments have the spatial resolution to resolve exoplanets from their host star. This enables direct characterization of the exoplanets atmosphere, but most direct imaging instruments do not have spectrographs with high enough resolving power for detailed atmospheric characterization. We investigate the use of a single-mode diffraction-limited integral-field unit that is compact and easy to integrate into current and future direct imaging instruments for exoplanet characterization. This achieved by making use of recent progress in photonic manufacturing to create a single-mode fiber-fed image reformatter. The fiber link is created with three-dimensional printed lenses on top of a single-mode multicore fiber that feeds an ultrafast laser inscribed photonic chip that reformats the fiber into a pseudoslit. We then couple it to a first-order spectrograph with a triple stacked volume phase holographic grating for a high efficiency over a large bandwidth. The prototype system has had a successful first-light observing run at the 4.2-m William Herschel Telescope. The measured on-sky resolving power is between

*Address all correspondence to Sebastiaan Y. Haffert, shaffert@email.arizona.edu

†These authors share first authorship.

‡Sebastiaan Y. Haffert is a NASA Hubble fellow.

2500 and 3000, depending on the wavelength. With our observations, we show that single-mode integral-field spectroscopy is a viable option for current and future exoplanet imaging instruments. © *2020 Society of Photo-Optical Instrumentation Engineers (SPIE)* [DOI: 10.1117/1.JATIS.6.4.045007]

Keywords: astrophotonics; integral-field spectroscopy; exoplanets; adaptive optics.

Paper 20039 received Apr. 21, 2020; accepted for publication Dec. 9, 2020; published online Dec. 23, 2020.

1 Introduction

Exoplanet characterization often makes use of spatially unresolved spectroscopy of transiting planets. During the transit, light from the host star passes through the planet's atmosphere and leaves imprints in the starlight, which can then be analyzed to characterize the planet. This has lead to remarkable characterization of a wide variety of exoplanets.[1–3] The same technique has been applied to measure the direct emission from the planet, either thermal emission or optical reflected starlight, itself instead of the indirect signatures in the starlight.[4–6] These are very challenging observations, but they are within the current limits of technology for hot Jupiters. The main limiting factor for the detection of fainter exoplanets in unresolved spectroscopy is the overwhelming amount of starlight contaminating the planet signal, which has to be removed in postprocessing by complex time-series filtering algorithms.

Direct imaging instruments, such as SPHERE,[7] GPI,[8] or SCExAO,[9] are built to spatially resolve planets on large enough orbit from their host stars and often employ extreme adaptive optics (ExAO) systems and advanced coronagraphs. By employing ExAO, the influence of the star is greatly reduced by spatially resolving the planet, allowing for easier characterization of the planet. The coronagraph is then used in conjunction with an ExAO system to suppress the starlight, to enhance the contrast between the star and planet even further. After employing all these optical techniques, there is still residual starlight that leaks through the system due to imperfect adaptive optics (AO) correction and residual phase aberrations that create speckles which can appear as planets. Image processing techniques are necessary to remove these residual speckles to recover the planet signal.

While several giant planets have been directly imaged and spectroscopically characterized,[10–13] the number of directly imaged planets has been limited so far. The current generation of high-contrast imagers is sensitive to the small population of young self-luminous exoplanets on wide orbits.[14,15] More planets could be directly imaged if the sensitivity close to the star is improved. Most of the current direct imaging instruments are limited at angular separations smaller than $10\lambda/D$ (0.4 in. at the VLT in H-band)[16] by quasistatic-speckles, which are slowly evolving speckles. Postprocessing algorithms that depend on spatial diversity, such as angular differential imaging (ADI),[17] are not able to remove the quasistatic speckles (QSS) due to the limited spatial diversity at small angles.

The combination of high-contrast imaging with high-resolution spectroscopy can resolve the issues that both techniques face. The effective resolving power on which the QSS change is mainly dominated by the scaling of the PSF with wavelength. This occurs on a resolving power of $R_{\mathrm{QSS}} = \Delta\theta/(\lambda/D)$, where $\Delta\theta$ is the angular separation, λ is the central wavelength of observation, and D is the telescope diameter.[18] Observing speckles at 1 arcsec with an 8-m telescope requires a resolving power $R_{\mathrm{QSS}} \approx 40$. High-resolution spectroscopy can remove the QSS efficiently if the spectral features of interest are narrower than the width corresponding to the effective resolution of the QSS. This usually holds for atomic and molecular spectral lines, which have an intrinsic resolving power between 100,000 and 200,000. Because these features are so narrow, most spectrographs dilute them to the spectrographs intrinsic resolving power. This sets the requirement that the spectrographs resolving power needs to be much larger than the effective resolving power of the speckles ($R \gg R_{\mathrm{QSS}}$), which happens roughly around $R \approx 1000$ and anything above this resolving power is what we consider high-resolution spectroscopy in

this work. The combination of high-contrast imaging and high-resolution spectroscopy has been proposed several times already,[19–23] and only recently projects started to add this capability to high-contrast imaging instruments.[24–26]

While the high-contrast imaging instruments are lacking high-spectral resolution capabilities, there are several AO-fed medium- to high-resolution spectrographs (MUSE, SINFONI, OSIRIS, CRIRES). These instruments have been successfully used in the past years to characterize exoplanet atmospheres. The infrared observations of β Pictoris b[27,28] and HR8799[29–32] were used to detect the presence of several molecules, including water. Due to the high resolving power, CRIRES[27] were able to detect a rotational broadening of β Pictoris b. In the visible part of the spectrum, MUSE was used to characterize the Hα emission of the protoplanet PDS70 b,[12,13,33] and due to the high sensitivity, a second planet was found in the system.[34] The success of these observations shows that it will be worthwhile to add higher resolution integral-field spectroscopy to the current and next generation of high-contrast imagers.

In this work, we take advantage of several astrophotonics technologies developed in recent years[35–37] to create a large core count single-mode (SM) photonic reformatter. With additive manufacturing,[38] a microlens array (MLA) is three-dimensional (3D) printed on top of the fiber face[37] to efficiently feed the individual cores. An integrated photonic chip is used to rearrange the two-dimensional geometry of the multicore fiber (MCF) output into a pseudoslit that can be dispersed.[39] Because the fiber is single-moded, the spectrograph back end can be kept small. The proposed fiber link can be easily used to add higher resolution spectroscopic capabilities to current-generation ExAO systems as an upgrade.[40]

The spectrograph in this work uses an MCF with 73 cores and has a bandwidth ranging from 1 to 1.6 μm which was set by the properties of the available fiber (lower wavelength limit) and the available detector (upper wavelength limit). This spectral range contains interesting spectral features from molecules, such as methane, carbon monoxide, and water and accretion-driven emission lines from hydrogen and helium. The dispersing element of the multicore fiberfed integral field unit (MCIFU) is a custom triple stacked volume phase holographic grating (VPHG) that disperses the light into three orders with higher efficiency compared with conventional transmission gratings.[41] A schematic of the spectrograph is shown in Fig. 1. The prototype MCIFU was designed and built during the first half of 2019 and had its first light at the 4.2-m William Herschel Telescope (WHT) on La Palma behind the CANARY AO system[42] in July 2019.

In Sec. 2, we give a short overview of different image reformatting methods and discuss their advantages and disadvantages for high-contrast imaging. In Sec. 3, we describe the design, manufacturing, and characterization of the fiber link, which includes the 3D nanoprinted

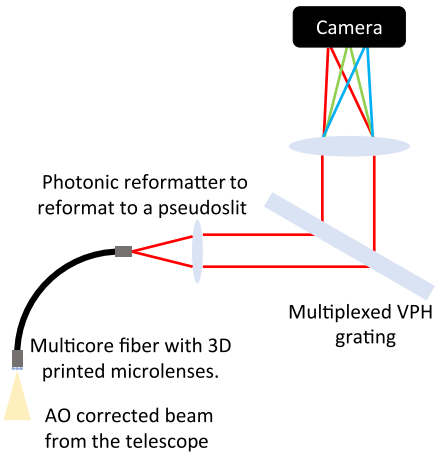

Fig. 1 An overview of the MCIFU. The telescope beam is imaged onto an MLA that is written on top of an MCF. The output of the MCF is rearanged into a pseudoslit by the photonic reformatter to make it dispersable. And finally, a triple multiplexed grating is used to disperse a broad wavelength range into three orders at a resolving power higher than $R = 5000$. The spectrograph itself is used in a first-order manner, where a lens is used to collimate the light onto a grating and a second lens is used to image the spectrograph focal plane.

MLA, the integrated photonic chip, and the fiber protection packaging. Section 4 describes the design and manufacturing of the custom VPHG, followed by the optomechanical design and characterization of the spectrograph with the VPHG in Sec. 5. Section 6 shows the first light results that were achieved with CANARY at the WHT. In Sec. 7, we discuss how to improve the current instrument for future use, after which the paper is summarized and concluded in Sec. 8.

2 Comparison of Image Reformatter Concepts for High-Contrast Imaging

An image reformatter is an optical component that rearranges an input focal plane into something that can be dispersed by a spectograph without losing spatial information. There are several options to achieve this: image slicers, microlenses, or fiber-fed spectrographs.

2.1 *Image Slicers*

An image slicer uses several reflective elements to reformat the field into a series of minislits. The image slicer creates the most efficient packing onto the detector, allowing for the most information to be recorded out of all techniques. But image slicers suffer from spatial–spectral cross-talk because adjacent spatial pixels along each slit are not separated on the detector. Another down-side is that the shape of the line spread function (LSF) changes depending on the the minislit illumination, which can occur, for example, due a slight tip or tilt of the input beam.[43] If high resolution spectroscopy (HRS) is needed to gain a large amount of contrast in postprocessing to characterize the planets, it is necessary to have a stable LSF because the HRS technique effectively searches for LSF variations across the field. If the contrast ratio that has to be bridged with respect to the local stellar halo is not very large (10^1 to 10^3), image slicers may be a good choice as previous observations have shown.[34,44]

2.2 *Microlens Arrays*

MLA-based integral field units (IFUs) use an MLA in the focal plane to sample the field. The MLA-based IFU is the current choice for spectroscopy on ExAO systems[7,45,46] and is even the standard observing mode for GPI.[8] An MLA IFU is easy to implement and is efficient when few spectral samples are required for large fields.[18] Another added benefit is that there are several ways to reduce the cross-talk between spatial-pixels by adding pinhole masks behind the MLA or aperture masks inside the spectrograph.[18] The reduced cross-talk allows the MLA-based IFUs to reach very deep contrast ratios of 10^4 to 10^6.[7,47] The drawback of the MLA IFUs is that it is not possible to measure many spectral resolving elements per spatial pixel (spaxel). Due to diffraction of the microlenses, the spot size is λF_{mla}, where λ is the wavelength and F_{mla} is the focal ratio of the microlens. Each spot requires an area of $\lambda^2 F_{\mathrm{mla}}^2$, while the total available area for each spaxel is the area of a single microlens, D_{mla}^2. That means that the maximum number of independent spectral elements is

$$N_\lambda = \frac{D_{\mathrm{mla}}^2}{\lambda^2 F_{\mathrm{mla}}^2}. \tag{1}$$

The relative bandwidth of the spectrograph is equal to the number of spaxels divided by the resolving power, $R = \lambda/\delta\lambda$, of the spectrograph,

$$\frac{\Delta\lambda}{\lambda} = \frac{N_\lambda}{\eta R} = \frac{D_{\mathrm{mla}}^2}{\eta R \lambda^2 F_{\mathrm{mla}}^2}, \tag{2}$$

where $\Delta\lambda$ is the spectrograph bandwidth and η is the detector filling efficiency. The usual range of η is between $1/2$ and $2/3$ to ensure either a separation of 1 or 2 resolving elements between the spectra, respectively. The equation as shown in this section holds for MLA-based IFUs with many spaxels where the spectra of the spaxels will overlap if the size of each spectrum becomes

to large. This is the case for most MLA IFUs in high-contrast imaging, which generally have several hundred lenses across the diameter of the field of view. If a smaller array is used, such as a 3×3 MLA, then the array can be rotated to create spectra without overlap and the derived equation does not hold.

The typical microlens diameter is on the order of 300 μm and for the near-infrared (NIR) a central wavelength of 1.4 μm is reasonable. If the microlenses have a focal ratio of 5, the total bandwidth that can be observed at a resolving power of 10,000 with a single exposure is 16%. The bandwidth reduces to 8% if the detector separation is included. For high-resolution spectroscopy ($R = 100{,}000$), the bandwidth becomes a factor 10 even smaller. The single-shot bandwidth is a crucial parameter for the HRS technique because the signal-to-noise ratio (SNR) of the template matching is proportional to the bandwidth and the integration time, SNR $\propto \sqrt{\Delta\lambda\Delta t}$.[19,22] If the single-shot bandwidth is not high enough, conventional imaging techniques, such as ADI, may be more efficient for exoplanet imaging.[48] The MLA approach would be very suitable to target a small bandwidth around emission lines, such as Hα, at high-resolution to search for protoplanets.

2.3 *Fiber-Based IFUs*

A field can be reformatted by feeding each spaxel into a fiber. A fiber bundle has the most flexibility of all reformatting techniques, and the input and output can be rearranged completely independent from each other. The fiber-based IFU was therefore also the first IFU concept to be used on-sky.[49] Most fiber-based IFUs until now have used multimode fiber (MMF). These fibers can capture all light due to their large core but have a low fill fraction due to their large cladding diameters. This problem has been reduced by feeding the fibers with a MLA to increase the field.[50] The past few years have shown that the mode filtering capabilities of single-mode fibers (SMFs) can be used to create coronagraphs with smaller inner-working angles or higher throughput.[51–54]

In addition, SMFs can reject random speckles from the ExAO system to increase constrast,[51] which has been used before in the interferometry community to make it easier to interfere different beams.[55,56] Because SMFs only propagate an SM, the LSF is also very stable, which will make it easier to calibrate the spectra. SM spectroscopy is currently pursued in the radial velocity field,[57] because the LSF from multimode fibers is not stable enough.[58] And as a final benefit because SMFs only allow the propagation of an SM, any incoherent source that consists of many modes will be attenuated.[59] This property is very desirable especially in the infrared where the thermal background from the sky is high and limits the SNR of most observations. Therefore, an SMF bundle provides a significant amount of benefits over other manners of image slicing, making it a very attractive option for high-resolution broadband integral-field spectroscopy. It is difficult to quantify the gain of an SMF IFU over other methods without complete end-to-end simulations, which include complete modeling of the instrument, calibration, and observing modes. A downside of SMFs is that the mode filtering capability is restricted to focal plane samplings of $1\lambda/D$ per spaxel or larger. If the spatial sample density is increased, the mode filtering becomes less effective, which removes the main benefit of the SMF. From this, it follows that an optimally designed SM IFU will most likely not Nyquist sample the focal plane, which will remove the ability to use postprocessing techniques, such as ADI. But with the addition of high-resolution spectroscopy, it is possible to apply postprocessing techniques, such as molecule mapping[28] or high-resolution spectral differential imaging,[34] to discover and characterize exoplanets.

2.4 *MCIFU Reformatter*

To reach a high field filling fraction, the SMFs have to be fed with microlenses.[52,60] SMFs have very strict requirements on the alignment of the fibers for efficient injection,[61] even more if they need to be combined with coronagraphy.[62] Currently, the only SMFs-fed IFU is RHEA,[63] which uses a bundle of SMFs that are fed by a bulk MLA. Accurate alignment of the SMF bundle behind the MLA is very difficult with typical depths of focus of 10 to 20 μm and lateral alignment tolerances ≤ 1 μm.[24] And even in case that the individual fibers would be aligned for high injection efficiency, getting the output of the fibers aligned in the same plane of focus for the

spectrograph is still difficult.[24] Both issues can be solved using MCFs, which contain several independent SM cores inside a single fiber. This ensures that the fibers are in the same input and output planes. But because of the small size of the MCFs, it is difficult to feed them with a bulk MLA and reach the required alignment accuracy. We will use *in-situ* 3D printing of the MLA directly on top of the fiber face, which will allow for much more freedom. However, due to fixed core spacing, it is difficult to disperse the output over a broad bandwidth if there are many cores.[64] The pitch constraint is similar to the constraint of microlens-based IFUs.[18,43]

3 Single-Mode Multicore Fiber Link

The fiber link allows the point spread function (PSF) from the AO system to be coupled to the spectrograph. A description of all the different elements of the MCIFU is shown in Fig. 2. Figures 2(a) and 2(b) show a schematic and photograph of the full MCIFU, with the five main components: (c) the MLA, (d) the MCF, (e) the MCF glued inside a custom V-groove, (f-g) the reformatter, and (h) an ultrafast laser fabricated mask to block unguided light in the reformatter. Finally, Figs. 2(f) and 2(g) show a schematic representation of the reformatter with the color scheme to distinguish each row of waveguides.

The fiber link was assembled by first manufacturing and connectorizing the MCF and chip, then aligning and gluing to the reformatter and mask which were manufactured using ultrafast laser inscription (ULI). This was then packaged using off-the-shelf and 3D printed components and finally the microlenses were printed on the MCF which was secured in an FC-PC connector. The following sections are arranged in the order of manufacture.

3.1 *Fiber*

Due to cost and time constraints, we used an already available MCF that had been manufactured for a different project. Therefore, the specifications and the geometry of the fiber were fixed. The MCF is comprised of 73 step-index Ge-doped cores manufactured using the common stack-and-draw fiber fabrication technique [Fig. 2(d)]. The MCF has a outer cladding diameter of 560 μm.

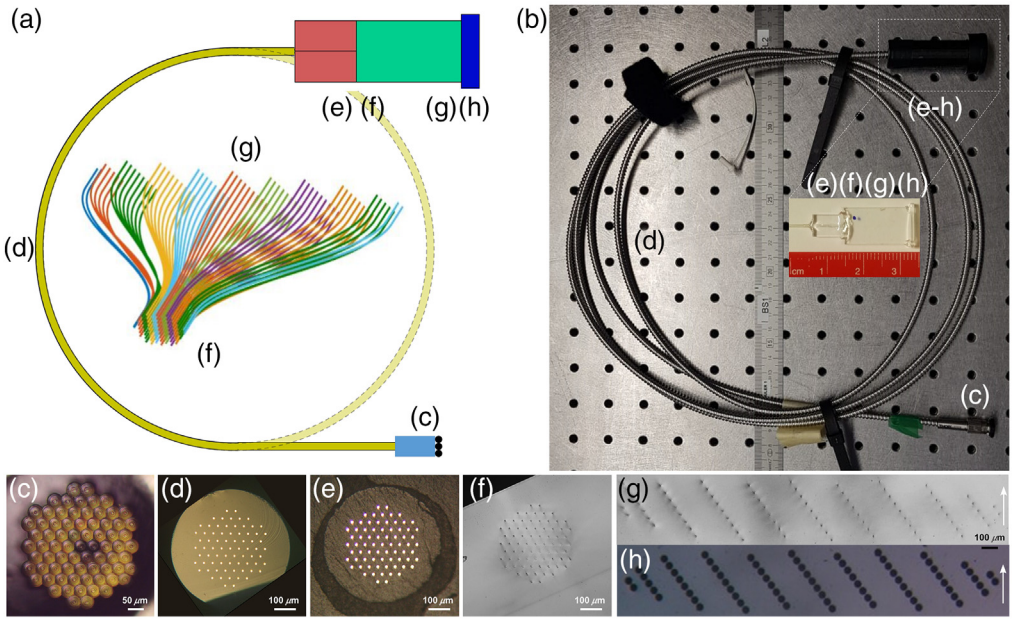

Fig. 2 The MCIFU fiber link, with important sections shown. (a) A schematic representation of the fiber link, (b) photograph of the complete packaged fiber link comprising all the elements from the MLA, (c) the 3D printed microlenses, (d) the bare fiber, (e) the bare fiber in a v-groove, (f) the input of the chip reformatter. (g) The output of the reformatter. (h) The output mask. The white arrow in (g) and (h) indicates the dispersion direction. Inset in (b): Scale picture of the full reformatter.

Each individual core has a numerical aperture (NA) of 0.14 and a diameter of ∼5.3 μm, which results in a mode field diameter (MFD) of ∼8.2 μm at a wavelength of 1.4 μm. The SM cutoff of each core is ∼970 nm. The cores are spaced by 41 μm, this means they are separated by approximately five times the MFD, ensuring negligible cross coupling between the cores.

3.2 *Reformatter and Mask*

At the spectrograph end, the MCF is directly butt-coupled to an ULI-fabricated 3D waveguide reformatter, which spatially reformats the MCF cores into a suitable arrangement, such that the dispersed spectra from each waveguide do not overlap with each other on the detector. To minimize undesirable effects due to scattered/unguided light not contained within the reformatter cores, a mask was fabricated using femtosecond laser inscribed chemical etching (FLICE). This mask consisted of a fused silica fixture with holes precisely positioned to align with the output waveguides. Measurements taken after coating the silica with a layer of chromium show that the chromium mask is blocking the stray light by a factor of 10 to 100 (see Fig. 3).

To separate the spectra from each MCF core and avoid any overlap after dispersion, the quasi-hexagonal MCF shape must be reformatted [Fig. 2(g)]. Existing reformatters have generally chosen a linear pseudoslit output pattern.[36,39,65] However, for the MCIFU, we chose a staggered slit. This has the advantage of increasing the spacing between adjacent cores, reducing cross coupling, while also reducing the translation of the waveguides within the glass. The reformatted pattern was created to give a spacing of 30 μm between the individual spectral traces of each core on the spectrograph. To do so, ULI was used to inscribe a reformatter in a $20 \times 10 \times 1$ mm borosilicate glass substrate (Eagle XG).[66] The inscription laser source is a MenloSystems BlueCut fiber laser emitting at 1030-nm a 500-kHz train of 350-fs pulses which are focused within the substrate with a 0.55-NA aspheric lens. Each waveguide was inscribed using a substrate translation speed of 8 mm/s and 19 scans of the laser focus with an interscan separation of 0.2 μm. This resulted in highly symmetric SM waveguides with an NA of ≈0.11 and MFD of ≈7.3 μm at the $1/e^2$ beam size of a Gaussian beam at 1310 nm. ULI has a limit in the refractive index contrast that can be achieved, which resulted in a lower NA of the ULI waveguides as compared with the NA of the MCF. This will lead to coupling losses at the interface of the reformatter and the MCF that represents a significant part of the global insertion losses of the reformatter. A custom MCF with an NA that matches the ULI specification would allow for a higher throughput. The pulse energy providing the highest throughput waveguides at the initial depth of 470 μm was 128 nJ and adjusted to 105 nJ for depths lower than 130 μm to compensate for spherical aberrations on the beam.

The waveguides were characterized by two different laser sources: a 1310-nm laser and a supercontinuum with an 1100-nm bandpass filter [with a full-width at half-maximum (FWHM) of 10 nm]. The two different sources were coupled into an SMF-28 optical fiber and characterization performed by butt-coupling the SMF-28 output to a single core of the MCF. The MCF was then butt-coupled to each individual waveguide of the reformatter with the aid of an index

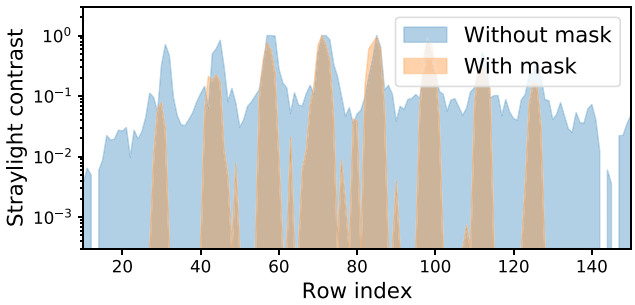

Fig. 3 A slice along one of the rows of the reformatter showing the scattered light with and without the chromium mask. Here, the input MLA is overfilled, specifically to simulate background light in astronomical observations. The blue shaded area shows where the scattered light is still detectable between the waveguides, the red shaded area shows the stray light with the mask. The row index is the pixel index along the extracted slice.

matching fluid. By this way, we ensure to work with the exact MFD to characterize the waveguides. SM behavior of the waveguides in the J-band between 1.1 and 1.3 μm was observed. The throughput was characterized with the ultrastable laser at 1310 nm. With this optimized set of parameters, the throughput of the straight waveguides can reach 67%, corresponding to a global insertion losses of 1.7 dB. To create the reformatter, an investigation was performed to optimize bend radius and minimize transmission losses. The bending losses are negligible for a bend radius in the propagation direction of >15 mm, deviating by a distance of 1 mm (corresponding to the extreme edge waveguides), and we have chosen a bend radius of 18 mm.

The final reformatter was permanently glued to the MCF using a UV curing adhesive. To provide a larger gluing surface to bond the fiber to the reformatter, a fiber support chip was fabricated with a custom hollow-cylindrical V-groove to house the MCF. This was created by the process of FLICE, in an ($8 \times 6 \times 2$ mm) fused silica substrate.[67] The V-groove shape was defined by the process of ULI with 200-nJ pulses from the Bluecut fiber laser at a repetition rate of 250 kHz and a subsequent wet chemical etch in 8 mol.L^{-1} potassium hydroxide solution at 85 deg to remove the excess material.

Finally, a mask was developed to block stray and scattered light at the reformatter output while allowing the light from the individual waveguides to propagate as desired. The scattered light in the ULI glass substrate can present a significant challenge for astronomical instruments trying to overcome the high contrast between the observed star and the planet.[68] The mask [Fig. 2(h)] was created by the process of FLICE in a similar manner to the fiber support chip from a $2 \times 12 \times 2$ mm-fused silica substrate. The high precision stages enabled a rectangular slot to be created to snugly fit the reformatter within this mask, with 30 μm diameter through holes precisely passively aligned to the waveguide positions [Fig. 2(g)]. A 120-nm layer of chromium metal was deposited on the outer surface of the mask by electron-beam physical vapor deposition. This process creates an opaque component that removes the scattered light present in the glass between the waveguides. Figure 3 shows the removal of scattered light between the ULI waveguides without and with the opaque mask in blue and red, respectively. The scattered light was measured by taking a slice along one of the rows of the reformatter.

In Fig. 4, we present the end-to-end throughputs from the MCF to the mask, at 1310 nm, before the MLA was added. In Fig. 4, one can clearly see that the fiber link has lost a significant part of the throughput on the top/bottom edges of the reformatter. These losses come from a slight variation of the input waveguide positions of the reformatter [Fig. 2(f)] in comparison of the MCF, inducing mode-field diameter mismatching. The high sensitivity of the coupling losses between the MCF and the reformatter is highlighted for our final device by a slight misalignment that can change the throughput from 67% to lower than 5%.

The whole output device was then encased with a combination of off-the-shelf components and 3D printed parts, and the MLA was secured within an FC-PC connector to create a robust component for use at the telescope [Fig. 2(b)].

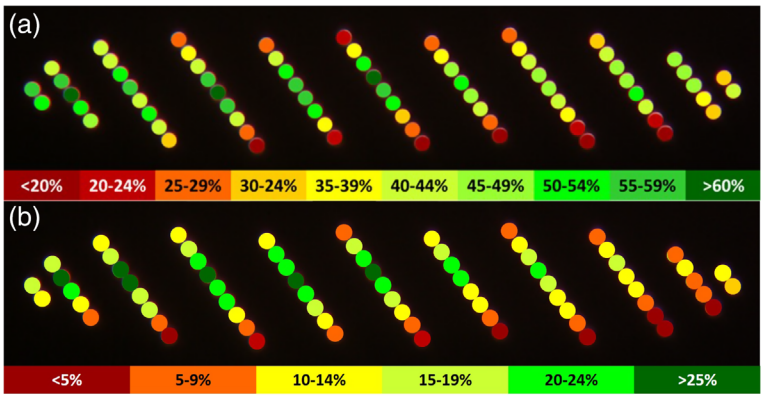

Fig. 4 Illustration of the measured monochromatic (1310 nm) throughput results for the fiber link. (a) The throughput for the 73 individual cores through the fiber, the reformattter and the chromium mask. (b) as for (a) but for the full fiber link, including the microlenses. The color bars represent the throughput ranges for each figure.

3.3 *Microlens Array*

The surface shape of the MLA was optimized for coupling efficiency using the physical optics propagation module in Zemax. To simulate the Airy pattern of a telescope, we used an unobstructed aperture with a diameter of 1 m. The beam was focused by a paraxial lens with a focal length that created a focal ratio of 22, allowing a $1.5\lambda/D$ sampling per microlens of the focal plane at 1.3 μm. The microlens surface was then modeled as a single lens with a hexagonal aperture made from IP-DIP.[69] We tried several freeform shapes to increase the coupling efficiency but found that there was very little improvement, less than a percent point, compared with purely spherical surfaces. Therefore, we chose a spherical surface for the final design. We found that a radius of curvature of 74.5 μm with a 205-μm height provided the highest wavelength averaged coupling efficiency of 67.5% to a single core of our MCF. Figure 5 shows the on-axis coupling efficiency as a function of the wavelength. The proposed microlens design has a theoretical wavelength-dependent throughput between 50% and 81%. The limiting factor in the throughput is the fraction of the Airy pattern that a single microlens captures. Due to scaling of the Airy pattern with wavelength, longer wavelengths will capture a smaller fraction of the PSF. The orange line in Fig. 5 shows the fraction of the transmitted flux for a microlens as a function of wavelength. It is clear that the coupling to the SMF cores is between 80% and 95% efficient across the spectrum, which shows that there will be little to gain from more complicated designs for on-axis objects.

The MLA was *in-situ* printed on the flat facet of the FC-PC connector in which the cleaved MCF was manually glued and then polished. The lenses were printed in a single block and in a single two-photon lithography step out of the commercial negative-tone photoresist IP-Dip.[70] The structures were defined by an in-house built lithography machine, equipped with a 780-nm femtosecond laser. An in-house developed machine software was used for high-precision alignment and writing with high shape fidelity. Illumination of the fiber back end with a red LED together with machine vision was used to detect all 73 cores of the MCF and align the individual lenslets to the cores. Therefore, the full 3D-model is generated only after core detection to be able to compensate any slight location and pitch variation of the individual cores of the MCF. The individual models of the lenslets are then merged and at places of overlap, due to the slight spatial variation in the MCF cores, the highest surface is chosen. Slight tilts of the fiber facet due to mounting are detected as well and the structures corrected accordingly. The writing distances between subsequent lines and layers, i.e., both hatching and slicing distance, were set to 100 nm. No antireflection (AR) coating was added to the microlenses. This adds some losses due to Fresnel reflection, which is roughly 5%.

3.4 *Performance of the Fiber Link*

With the whole system assembled and packaged, the individual cores were tested for throughput. This was again performed at 1310 nm to be consistent with earlier tests. The light sources were fed through an SMF and then to a collimating lens (Thorlabs AC254-200-C). The collimated

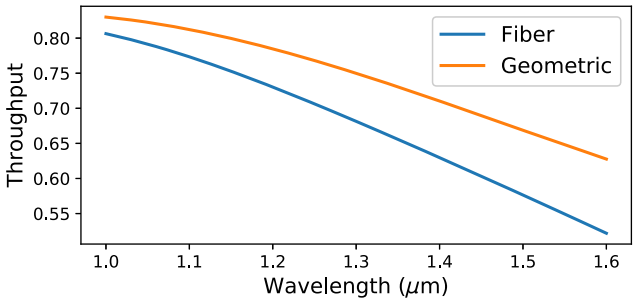

Fig. 5 The amount of on-axis light that couples into a single core of the MCF as function of wavelength within the spectrograph bandwidth. The fiber throughput is the amount that couples into a single core, while the microlens throughput is the amount of light that enters the microlens. With the MLA we can couple between 80% and 95% of the light that falls on a single microlens.

beam was stopped down by an aperture stop to simulate the same focal ratio of 22 beam that the foreoptics of the experiment with CANARY will supply to the microlenses. Finally, a lens (Thorlabs AC254-100-C) was used to focus the light onto the microlenses. To simulate the on-sky conditions, the input light was first optimized for position, focus, tip, and tilt using a central lens. This was optimized and checked at several points across the lens array and then used as the reference. Only from this point, the horizontal (x) and vertical (y) positions were changed, maintaining a global reference for all the microlenses. This means any deviation from perfect will reduce the throughput of the individual lenses. However, it better matches the expectations on sky conditions. This simple setup creates a diffraction-limited beam and shows the wavefront error-free throughput.

The recorded throughputs are shown in Fig. 4. This shows that the central cores performed best, with significant reduction at the edges. Causes and solutions are discussed in Sec. 7.

4 Triple Stacked Volume Phase Grating

The ultimate goal of the instrument is to have a spectral resolving power between 5000 and 10,000, which can be readily accessible with transmissive volume phase gratings (used in the first diffraction order with the present design). Despite this, even if VPHGs can be made with very high diffraction efficiency, the disadvantage of a classical, single first-order grating is that the light will be smeared out in a single spectrum, thus wasting usable portions of the detector. Moreover, for securing the large bandwidth at the target resolution, it is required to use a very wide sensor, which is very expensive and not readily available. A possible solution is to multiplex the VPHG in layers as reported in Ref. 41. In this way, each grating can diffract a different part of the wavelength range toward the same direction so the average efficiency is improved by a wide margin, by having more than one efficiency maximum. To separate the spectra on the detector plane, the gratings are rotated with respect to each other, with a designed angle set to have clearly separated spectra and output signals which are as horizontally dispersed as possible (see Fig. 6).

4.1 *Design*

Considering the working wavelength range for this application of 1000 to 1600 nm, the geometrical conditions have been chosen with the aim to obtain three first-order diffraction efficiency curves with maxima at around 1100, 1300, and 1500 nm, ensuring a high efficiency at each wavelength. The incidence angle defined in the spectrograph design is 21.5 deg. This angle is shared by the three dispersing layers and the grating line density has been chosen to match the Bragg condition at the central wavelength for each of the three gratings.

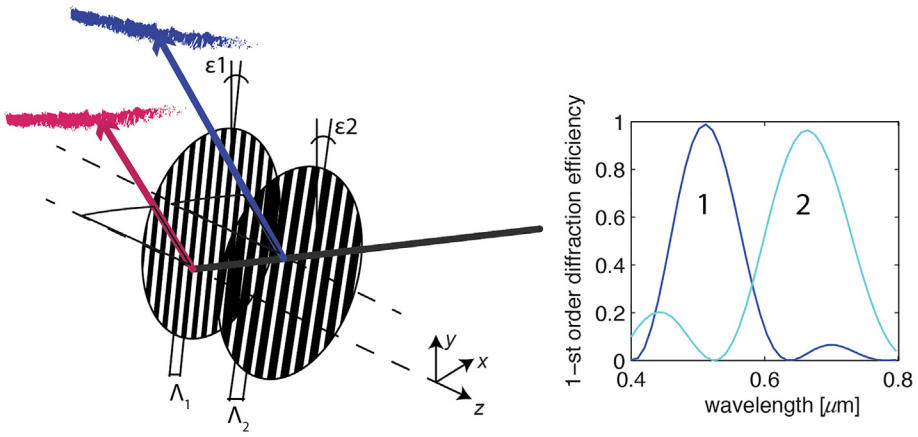

Fig. 6 Scheme of the spectral-multiplexing concept. For simplicity, a two-stacked VPHG is presented, each creating a separate spectrum which are shown in different colors. The inset shows the simulated diffraction efficiencies of the two layers for an example design.

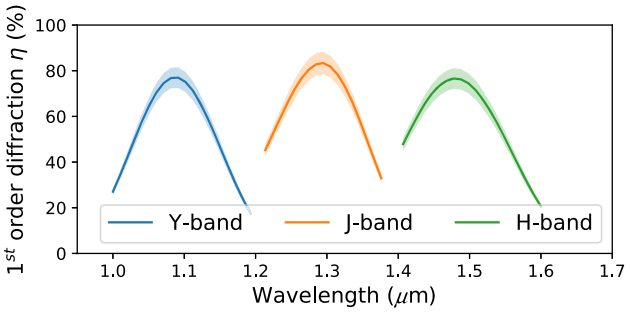

Fig. 7 Simulation of the combined diffraction efficiency of the multiplexed VPHG for an incidence angle of 21.5° for unpolarized light. The shaded area presents the minimum and maximum diffraction efficiency prediction for the manufacturing process. Material absorption and reflection losses have been estimated and taken into account.

Table 1 Main features selected for the three designed diffraction gratings.

Layer #	Central wavelength (nm)	Index modulation Δn	Layer thickness (μm)	Grating pitch (lines/mm)	ϵ rotational angle (°)
1	1100	0.022	28	668	−3
2	1300	0.020	34	565	0
3	1500	0.010	50	490	3

The efficiency and bandwidth of each single layer (and thus the refractive index modulation strength, Δn, of the grating and thickness of VPHGs, respectively) have been calculated and optimized by means of a rigorous coupled wave analysis-based script. The ad-hoc code takes into account the interaction between the diffractive layers and computes the final throughput of the multiplexed element, see Fig. 7. The losses due to reflection as well as those due to materials absorption and scattering have been considered in the simulations to have a reliable prediction of the efficiency curves. In Table 1, the final design parameters of the stacked optical element are reported.

4.2 *Manufacturing*

The choice of the materials with different thickness has been based on the Δn requirements along with the width of each first-order diffraction and the line density required for each grating. The three gratings have been produced using the Bayfol® HX material. This photopolymeric film has been chosen due to its ability to address precisely the required Δn values, simply selecting the proper writing conditions (e.g., laser power density).[71] Moreover, the solid layers can be used in a configuration that requires only one glass substrate in between the layers, resulting in a thinner diffractive element. Each VPHG layer composing the final device has been produced individually by means of the holographic setup based on a 532-nm diode-pumped solid-state laser. Every photopolymeric grating is supported by a BK7 round window (1 in.), the front and the back ones possess AR coating on the outer face (optimized from 1 to 1.6 μm at 21.5 deg).

After the characterization of each layer, they were coupled with index matching fluid (cedar oil) and aligned according to the tilt angles specified in the design phase. To hold and block firmly the three layers, an ad-hoc 3D-printed plastic (PLA) shell was used.

5 Spectrograph

5.1 *Optical Design*

The spectrograph was designed with off-the-shelf lenses. The output of the reformatter was estimated to have a focal ratio of 5, which was subsequently used as the input source for the

spectrograph design. The spectrograph design is a standard first-order design, with a collimator lens that creates the beam that will be dispersed by the grating, and a camera lens that focuses the spectra onto a camera. For the camera lens, we used an achromatic tube lens from Thorlabs, which has diffraction-limited performance over a large field of view and spectral bandwidth while also delivering a flat image plane. These properties make the tube lenses from Thorlabs ideal as camera lenses for integral-field spectrographs. From the available tube lenses, we found that the TTL200-S8 fitted within the requirements of the MCIFU.

The focal ratio of the waveguides ($\#F = 5$) together with the effective slit length of 2 mm required us to create a custom collimator. We used combinations of spherical singlets to create a "semicustom" collimator. The design procedure started with two off-the-shelf doublets. The internal interface of each of the doublets was set to flat (a radius of curvature of infinite). All four outer surfaces of these two doublets were optimized by minimized the angular root-mean square (rms). Then, the surfaces were iteratively replaced with the closest matching off-the-shelf singlet that was available from either Thorlabs or Edmund Optics and then the angular rms was minimized by reoptimizing the remaining surfaces. We repeated this procedure until we found a combination of singlets that had diffraction-limited performance over the full wavelength range and pseudoslit length of the reformatter. Even though the optical quality of this semicustom collimator was satisfying, not all optics were available with NIR optimized coatings. This resulted in a collimator with several uncoated optics that reduced the throughput. Figure 8 shows the total theoretical wavefront quality of the spectrograph design. Almost the full wavelength range is diffraction-limited, except for the small range of 1.0 to 1.03 μm which is nearly

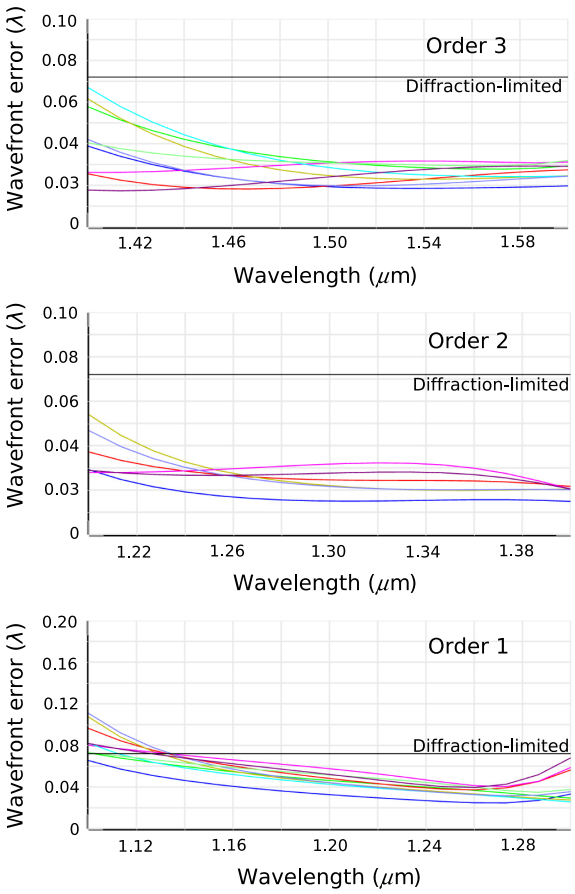

Fig. 8 The wavefront quality of the spectrograph as function of wavelength for the three different orders that are made by the VPHG. The various colors represent a position along the pseudoslit and are the same pseudoslit position for each order. Here, we can see that the spectrograph design is diffraction-limited over almost the full spectral bandwidth. Only the blue part of the Y-band is slightly nondiffraction-limited, which will lower the effective resolving power.

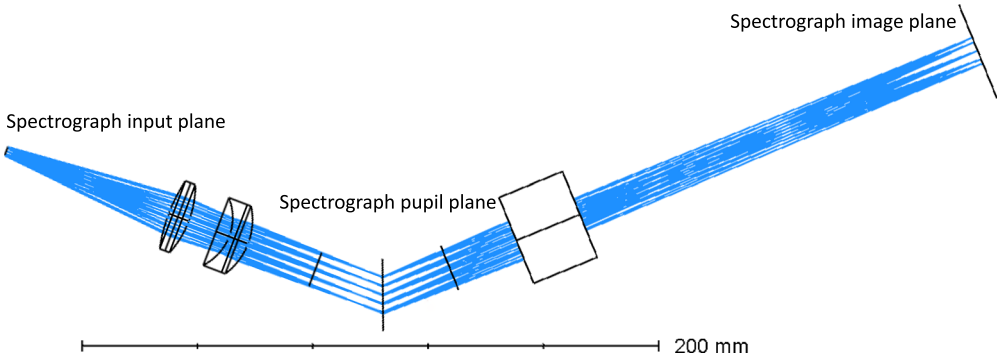

Fig. 9 The layout of the spectrograph with the different components of the spectrograph. The scale bar shows the small footprint of the optical path of the spectrograph, which is roughly 40 cm × 20 cm.

diffraction-limited. The final layout of the MCIFU spectrograph is shown in Fig. 9. The spectrograph could be kept small with a footprint of $\sim 200 \times 400$ mm due to the SM input.

The collimator creates an 11-mm pupil diameter, with <0.5 mm of pupil wander as a function of position along the pseudoslit. The diffraction-limited resolving power of the spectrograph is $R = W\rho$, where W is the projected size of the pupil onto the grating and ρ is the line density of the grating. The theoretical maximum resolving power would then be ~8000, 6700, and 5800 for Y-band, J-band, and H-band, respectively. For best performance, the spectrograph has been designed to work with an output plane of 2048×2048 pixels. A C-RED II with 640×480 pixels was available for the MCIFU tests. The complete spectral range was covered by translating the camera. The full spectrograph output is covered by 12 camera positions.

5.2 *Mechanical Design*

The mechanical design of the spectrograph (see Fig. 10) is simple due to its small size and the optical beam features (slow beams). Moreover, the simplicity was also a requirement due to budget and time constraints from the design to the commissioning. The working angle of the VPHG in respect to the collimator and the angle with the camera are set using two 3D printed

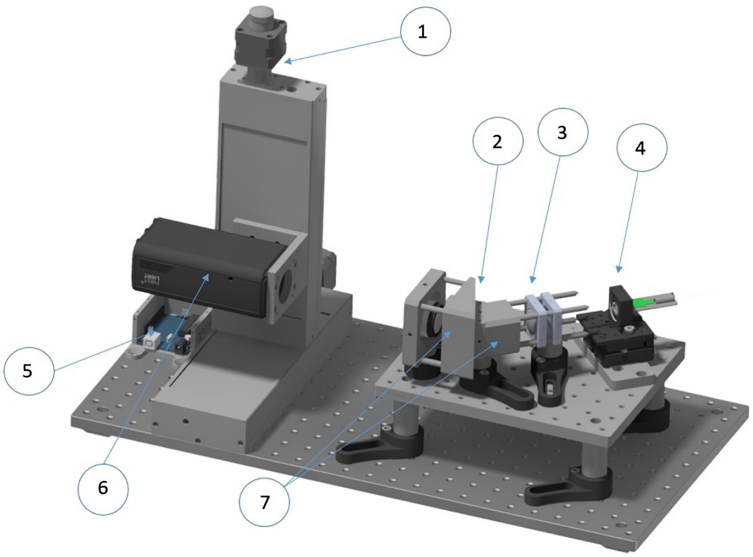

Fig. 10 Mechanical design of the spectrograph from the reformatter to the camera: (1) motorized stages, (2) dispersing element, (3) collimating optical elements, (4) reformatter holder, (5) Arduino control components, (6) C-RED 2 camera, and (7) 3D printed elements.

pieces, allowing for a simple integration and alignment procedure. The additive manufacturing approach was chosen also for the reformatter holder that allows for fitting the reformatted fiber inside a standard mounting. The degrees of freedom of this component are the tip-tilt, the decenter, and the focus. The motorized stages that carry the camera are the same that used in 3D printed setups and allows for covering the full field-of-view by a set of discrete positions.

5.3 *Performance*

After integration of the spectrograph, we characterized the throughput and resolving power of the spectrograph. To have a good estimation of the spectral throughput of the instrument, we used a tunable light source (TLS) (Oriel TLS-300X). The poor coupling between the faint TLS source and the fiber prevented a good signal/noise for the throughput measurement. To send some light through the instrument, we had to measure the subsystems independently and without the fiber. Moreover, as the $f/\#$ of the source did not match the instrument, we decided to first measure the Multiplexed VPHG, and then the in-line optical train without the VPHG.

The throughput of the spectrograph lenses was also measured with a 1064-nm diode laser, knowing that the spectral response is mainly due to the interface reflections it is consistent with the previous estimations. The throughput of the lenses in the spectrograph is ∼0.8 which is consistent with the fact that the first two lenses are not AR coated. The total throughput of the system is then calculated adding the VPHGs contribution. In Fig. 11, we report the spectrographs total throughput and the measured efficiency curves of the Multiplexed VPHG.

With all individual components measured, we can determine the total end-to-end throughput. The wavelength-dependent throughput is shown in Fig. 12. The throughput of CANARY with the WHT (T. Morris, private communication) is also included in the throughput budget. The impact of the AO performance on the coupling efficiency is based on the expected Strehl ratio of CANARY and simulations that determine the relationship between the Strehl ratio and fiber coupling efficiency.[61] From this, we determine that the expected end-to-end throughput is on the order of 0.4%. The main limitations are the fiber link throughput and the AO performance.

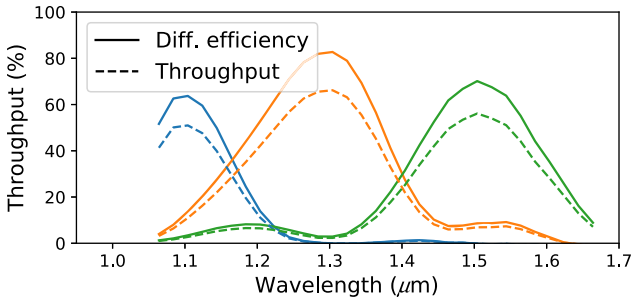

Fig. 11 The measured diffraction efficiency and throughput of the spectrograph without the fiber link as measured by the tunable laser source. The solid lines show the diffraction efficiency of the stacked VPHG system. The dashed lines include the throughput of the spectrograph optics.

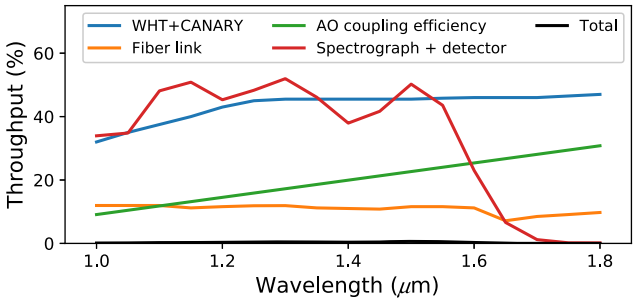

Fig. 12 Throughput of the individual components together with the total throughput (black). The largest limiting factor is the fiber link. The total throughput is 0.4% on average.

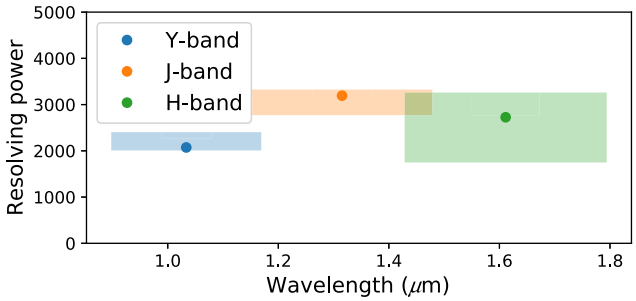

Fig. 13 The measured resolving power of the MCIFU for the three different spectral orders. The shaded area shows the 1-σ resolving power estimates from several emission lines within each order. The points in each area show the median resolving power of that order. The H-band resolving power has a large spread due to line blending of many of the measured lines. The estimated resolving power is a factors 2 to 3 lower than the theoretical limit.

The resolving power of the spectrograph was determined with a Krypton line lamp (Oriel 6031 Kr Spectral Calibration Lamp). To obtain a wavelength solution for all individual cores, we injected the light through the fiber bundle. Even though the line lamp was a large incoherent light source, we were still able to couple enough light into each individual core for the calibration purposes. The wavelength solution was fitted with a first-order polynomial. From the wavelength solution, we derived a linear dispersion of 0.070, 0.850, and 0.095 nm^{-1}. The measured dispersion of each of the gratings was within 1% of the designed dispersion, indicating that the triple stacked grating was manufactured within specifications. From the line lamp measurements, we could also derive the effective resolving power of the spectrograph, which is defined as the center wavelength of the Kr emission lines divided by their FWHM. The resolving power for the different spectral orders is shown in Fig. 13. The effective resolving power is a factor 2 to 3 lower than expected. This is most likely due to a misalignment of the collimation optics, as the PSFs of each emission line are magnified more than expected, show an asymmetry, and have a strong Airy ring. An example of the PSFs which contain these effects can be seen in Fig. 14.

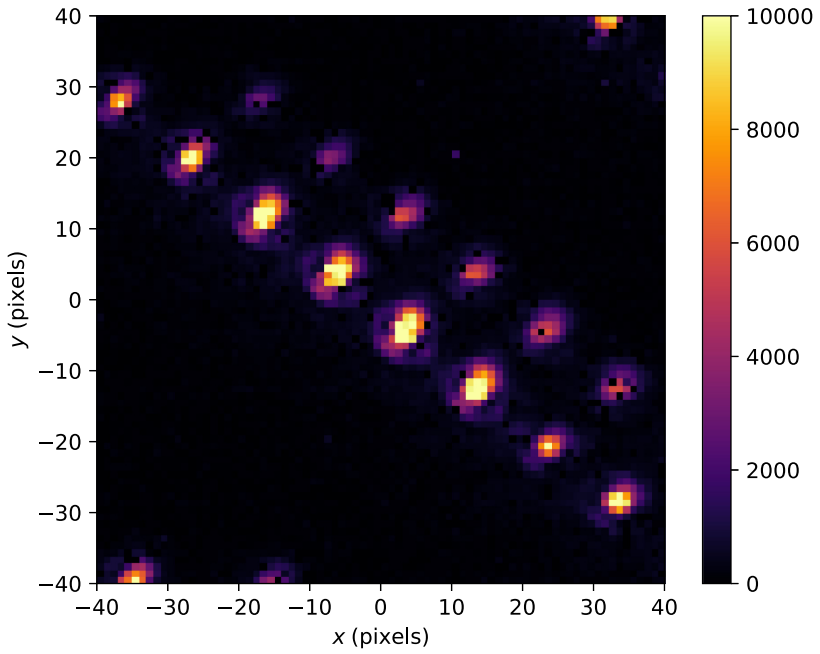

Fig. 14 The PSFs of the spectrograph as measured with the Kr spectral calibration lamp. The horizontal axis is the dispersion axis. The diagonal array of PSFs is the output of a single emission line illuminating a single row of the reformatter. The PSFs are extended and asymmetric toward the north-east and show a clear Airy ring.

These features are not expected from SM waveguides that output Gaussian-like profiles and indicate that we are vignetting the beam inside the spectrograph.

6 Testing with CANARY

The spectrograph was tested with the CANARY AO system at the WHT.[42] CANARY is an AO demonstration test bed for wide-field laserguide star tomography and open-loop AO control. The main purpose of such an AO system is to deliver good wavefront correction over a large field of view. CANARY was used in single-conjugate adaptive optics mode for the MCIFU experiment. In this mode, the wavefront errors are measured by a 7×7 Shack–Hartmann wavefront sensor, which are then fedback to a 52-element deformable mirror (DM) and dedicated tip-tilt mirror. In this configuration, CANARY delivers a Strehl of 30% in nominal atmospheric conditions in H-band. The data were taken between 18 and 21 July, 2019, under the OPTICON open access time. This time was shared with two other groups performing experiments, dividing the nights into sections.

Once assembled, the MCIFU was tested using the internal CANARY sources. We used a modified simulated annealing routine[72] to remove path abberation between the wavefront sensor and the fiber. The algorithm optimized the shape of the DM, maximizing the fiber coupling. This increased the fiber coupling by $\sim$10%.

Several exposures with increasing exposure time were taken to create a high-dynamic range image for the postfiber contrast determination. The postfiber contrast map is shown in Fig. 15. The contrast in the first ring is on the order of 10^{-2}, which is similar to the contrast of the first Airy ring. The map also shows that there is some asymmetry in the PSF. The asymmetry in the contrast map hints on residual astigmatism or coma, which is on the order of 0.5 rad rms by comparing the simulated contrast maps with the data, which is shown in Fig. 15.

6.1 *On-Sky Performance*

Once on-sky, we targeted bright stars to estimate the performance. Our prime target was Vega, because we could use it as a calibrator star. In Fig. 16, the full spectrograph output is shown by a stitched image of 12 camera positions. Due to the AO tip-tilt variation and because the exposures of the individual camera positions were taken sequentially, there is some variability in the flux between the positions. Not all cores of the MCF could be used during the on-sky demonstration as there was not enough separation between the three orders to fit all the 73 cores, which resulted in overlapped spectra. The top and bottom of the reformatter was blocked with a mask to remove the overlapping spectra.

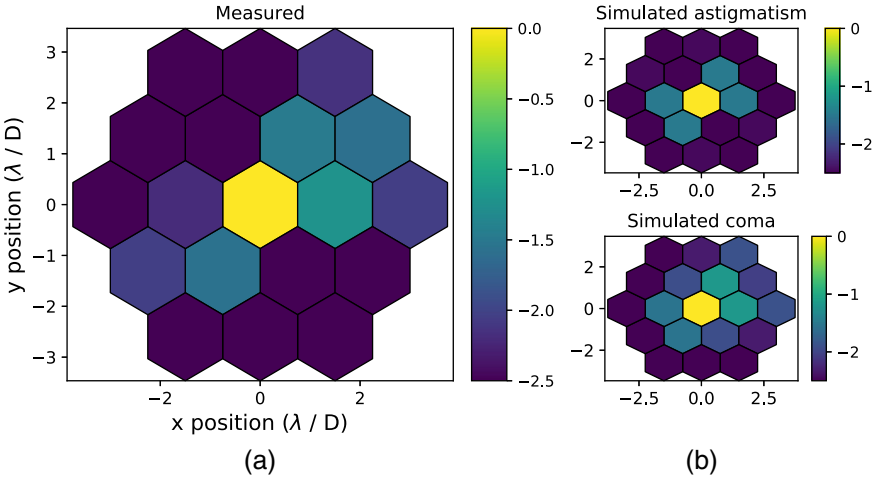

Fig. 15 (a) The monochromatic post-fiber contrast map on a logarithmic scale as measured with a 1550-nm laser. (b) A comparison of the asymmetry in the illumination with simulations hints on the presence of 0.5-rad rms residual astigmatism and/or coma.

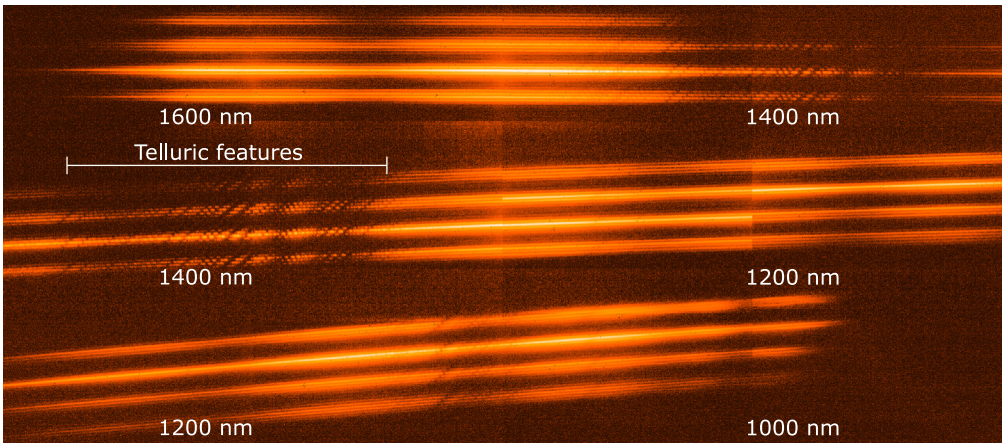

Fig. 16 The full spectrograph output of Vega after stitching 12 detector positions together. The color of the image is logarithmically stretched to highlight the spectra from the fainter fiber cores. Each fiber captures a different part of the PSF at the input, therefore the brightness of the spectral trace corresponds with the brightness of the captured part of the PSF. The main features that are visible are the telluric lines imprinted into the spectrum of Vega. Abrupt changes in the continuum of the individual cores are visible because the full image was reconstructed from 12 observations that were taken one after another, with varying conditions. The beginning and end of each spectrum has been marked with the corresponding wavelength.

Vega is an A0 star which means that it is almost featureless, the main spectral features that are visible come from the Earth's telluric absorption lines. Figure 17 shows the extracted spectrum from 1310 to 1390 nm averaged over all fibers. We chose this part of the spectrum as it illustrates the effect of the telluric features. The telluric features allowed us to do an independent measurement of the on-sky resolving power and wavelength solution. We used the ESO SkyCalc[73,74] to generate a transmission spectrum using the standard Paranal atmospheric parameters. Vega was modeled with a high-resolution PHOENIX stellar model[75] with an effective stellar temperature of $T_{\mathrm{eff}} = 9600$, metallicity of $Z = -0.5$, and surface gravity $\log\, g = 4.0$. We used a fourth-order polynomial for the instrument throughput and also used a fourth-order polynomial for the wavelength solution. The high-resolution spectrum was convolved by a Gaussian with a certain width to mimic the effect of the spectrograph resolving power. The retrieved resolving power from this procedure was $R = 2970$, which matches very well with the estimated resolving power from the Kr line lamp. We did not match all features in the observed spectrum because the parameters of both the telluric model and the stellar model were fixed. The good match between the measured and modeled spectra shows that we can extract high fidelity spectra that are not contaminated by etalon and fringing effects. Previous SMFs spectrographs were plagued by strong etalon amplitude variations, which could be up to 10% across the spectra.[24,63]

Because of the optical layout of CANARY and the MCIFU, it was not possible to image the PSF and the spectrograph output. Therefore, we were not able to get a direct estimate for the on-sky fiber coupling efficiency.

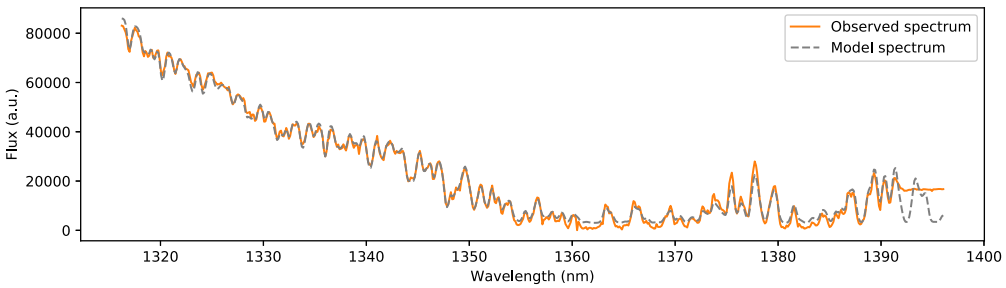

Fig. 17 The spatially averaged spectrum of Vega from 1300 to 1400 nm. The structure of this part of the spectrum of Vega is predominantly caused by the telluric absorption lines.

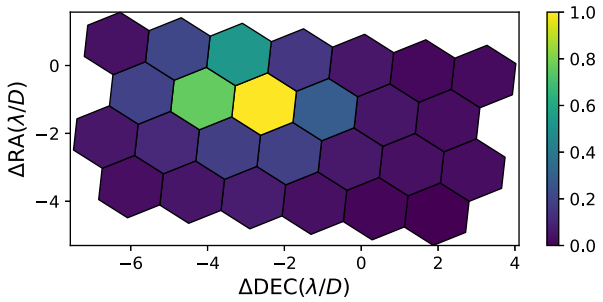

Fig. 18 The on-sky reconstructed H-band image, using the MCIFU, of the bright star Alpha Herculis. The observations were taken at 10 Hz. The image shown here is the mean of 1000 successive images from the data stream. Each microlens samples roughly $1.3\lambda/D$. The asymmetry in the PSF comes from a slow drift in tip/tilt alignment during the observations.

A second target that was observed was Alpha Herculis, one of the brightest infrared targets in the sky with magnitudes of $J = -2.3$ and $H = -3.2$.[76] The brightness of the target allowed us to do high-speed integral-field spectroscopy at 10 Hz, at a single camera position. In Fig. 18, we show the reconstructed H-band PSF of one of the exposures.

During the OPTICON July 2019 run at the WHT, another experiment was performed to characterize AO performance with a more sophisticated controller, the linear quadratic Gaussian (LQG) regulator instead of the standard integrator. The LQG regulator relies on a model that describes the temporal dynamics of the disturbance and whose relevance is a key for a performance improvement. It includes both the autoregressive order 2 model on the first 495 Zernike modes built from turbulence priors as described in Ref. 77, and a data-driven model for the nine first modes estimated from recent AO telemetry data. This LQG controller provides a more accurate modeling of the temporal dynamics for the most energetic modes: not only vibrations on the tip and tilt but most of other sources of disturbance on the nine first modes is captured whether it comes from dome turbulence, windshake, or atmospheric turbulence. Implementing this, LQG controller required very little tuning and proved to deliver increased performance and to be much more stable than the integrator.[78] During the night from 21st to 22nd July, 2019, we observed Alpha Herculis both with the integrator and the LQG and measured the impact on the tip-tilt residuals. To estimate the performance, we made a white light image of the IFU PSF and calculated the centroid of the white-light PSF as function of time. The centroid was measured using the center-of-mass of each PSF. We estimated that the LQG successfully decreased the standard deviation of the centroid by a factor of $\sim$1.4.

7 Discussion

The on-sky tests of the MCIFU have shown that the components are able to work together on-sky to deliver an SMF-fed NIR integral field spectrograph (IFS). It was not possible to optimize the performance of all components due to the short time (6 months), between inception of the instrument and the on-sky demonstration. Because the MCIFU is modular, it is possible to redesign and optimize individual components and switch them for better performance. There are several parts that we have identified that can be improved with a clear path.

7.1 *Fiber Link Improvements*

Our complete fiber link system showed throughput of between a few and 27% for individual cores. As this fiber link was a new system developed in only a few months, we are happy with its initial performance. For future experiments, we will develop a new fiber, with the aim of increasing both throughput and uniformity. Our target is to bring the fiber link throughput much closer to 50%. To achieve the increase in the performance for our new reformatter, we will need to improve our ability to accurately control the inscription to create a better mode matching between the cores and to optimize their alignment. A shorter pulse laser can allow us to optimize

the laser–matter interaction in the substrate and enhance the inscription accuracy. By this way, we expect to increase the throughput for the straight waveguide and enable a more precise alignment of the MCF with the ULI wavguides to avoid the variations in throughput seen in Fig. 4.

Further improvements in practical coupling efficiencies by the microlenses should also be possible as we keep developing the manufacturing process. Past work/experiences have shown that the coupling efficiency that can be achieved in the lab is close to the theoretical modeling. Yet, the current microlenses were higher and printed over a much larger surface than normal, likely effecting performance of the outer lenses. The most probable cause is shrinkage of the structure during the curing step. Shrinkage has a stronger effect on the outer cores than the inner cores. Thus, further optimization and refinement/iterations need to be made to improve efficient coupling. And finally, an AR coating can be added to the microlenses to get the highest possible throughput.

7.2 *Spectrograph Improvements*

The triple stacked VPHG shows a performance close to the theoretical design limit. This indicates that we are operating at the current manufacturing limit of the VPHG technology. The main limiting factor in the spectrograph is the collimation optics. The alignment of the separate singlets is quite sensitive, and there is quite a large loss of throughput due to the uncoated optics. Both the throughput and the resolving power can be improved by a redesign of the collimation optics.

7.3 *New Detector*

Currently, a C-RED 2 is used as a detector for the MCIFU. The C-RED 2 is designed for a small field of view high-speed NIR imaging and not long-integration spectroscopy. Due to the high read noise and dark current of the C-RED 2, the single spectral channel limiting magnitude in 1 h is about 12th magnitude at the WHT if we exclude the contributions from the background. Combining all spectral channels could improve this to about 15th magnitude. Because of the low number of detector pixels, we need to scan the spectrograph focal plane in several steps, which as shown in this work makes postprocessing more difficult due to tip-tilt stability. Ideally, we would use a detector with 2 k $\times$ 2 k pixels and low read and dark noise. Currently, the best available solution for us would be a HAWAII-2RG,[79] though we also note the increasing pixel numbers on SAPHIRA detectors and a 2 k $\times$ 2 k version would make a very attractive solution. Switching to a HAWAII-2RG would increase the limiting magnitude by five magnitudes.

7.4 *On Sky*

CANARY is an AO demonstration test bed for wide-field laser guide star tomography and open-loop AO control. For high-contrast imaging of exoplanets, we need to use ExAO systems that focus only on a very small field of view around the star. For SMF optics, this reduces the coupling into the fiber which is proportional to the Strehl.[61] For our observations, the estimated on-axis Strehl from CANARY was between 5% and 15% in the H, which will be lower in the J band. The Strehl was lower than expected due to poor atmospheric conditions. This shows an advantage of integral-field spectroscopy as opposed to single-object spectroscopy where the full PSF is injected into a single SMF.[26] Due to the microlenses and multiple fiber, the MCIFU is much less sensitive to pointing errors and residual tip/tilt errors. But adding the MCIFU behind an ExAO system that delivers high Strehl in the NIR such as the Magellan Adaptive Optics Extreme (MagAO-X) system[80] would allow for much higher coupling into the fiber. Due to the high Strehl, it would also be possible to use high-performance coronagraphs to reduce the amount of starlight that pollutes the planet signal. The past few years have shown that with SMFs it is possible to make higher performance coronagraphs.[51–54,62]

We reckon that after implementing all proposed upgrades, the throughout can be significantly increased. An overview of the current and target throughput for each subsystem is shown in Table 2. For the current system, three components are significantly limiting the throughput, the AO performance, the microlens coupling, and the reformatter. The throughput can be increased

Table 2 Wavelength averaged instrument throughput.

Subsystem	Current	Optimal	What to improve
WHT + CANARY	0.43	0.43	
Microlenses absorption	0.90	0.96	Thinner microlenses
Microlens alignment	0.3	0.9	More development time
AO coupling	0.2	0.66	Switch to ExAO system with Strehl above 90%
Reformatter	0.4	0.7	Refinement of the manufacturing
Spectrograph	0.8	0.9	New AR coatings
VPH	0.5	0.6	Refinement of the manufacturing
Detector	0.8	0.9	Switch to HAWAII-2RG
Total	0.003 (0.005)	0.07 (0.11)	Peak throughput in brackets

by a factor close to 20 if only these three components are addressed, which shows the importance of further refinement of the fiber link and future tests on ExAO systems.

8 Conclusions

Here, we present the MCIFU an innovative prototype SMF-fed IFS designed to characterize exoplanets that can easily be added to existing and future high contrast imaging instruments. The PSF from an AO or ExAO system is focused on a 3D printed MLA which feeds an MCF. At the entrance to the spectrograph, the output slit is formed using an ULI reformatter. The spectrograph itself is formed from off-the-shelf components, 3D printed components, a custom set of triple stacked VPHGs, and a C-RED 2 detector. The prototype instrument itself went from design to telescope in $\sim$6 months. Due to its modular nature, the instrument can be easily upgraded and adapted for observations with other AO systems.

The SMF link has been demonstrated to work on-sky, even in low Strehl conditions which are challenging for instruments where the full PSF is injected into a single SMF. We derived a resolving power consistent with our lab measurements from the telluric lines in the observed spectrum of Vega. And furthermore, we demonstrated that it is possible to get high-speed integral-field spectra with the current MCIFU. With our observations, we could confirm the improved performance of a new AO real-time control algorithm.

Both the fiber link and spectrograph performance are slightly less than half the theoretical maximum, with the fiber link throughput being around 20% and the resolving power being around 3000. This is due to the short manufacture and assembly time, and currently work is being done to improve and we plan to test the first modifications with MagAO-X. We will compare our results with those from CANARY and then begin a modular improvement program, bringing the system from prototype to full instrument.

Acknowledgments

We want to thank the referees for giving extensive feedback which has greatly improved our work. We thank B. Wehbe for sharing his knowledge of atmospheric dispersion and R. and D. Haynes for productive discussions about fiber preparation and packaging. We also thank the Network of Young Researchers in Instrumentation for Astronomy (NYRIA) network, for seeding the ideas and beginning the collaboration for this project. Sebastiaan Y. Haffert acknowledges funding from research program VICI 639.043.107, which is financed by The Netherlands Organisation for Scientific Research (NWO). Support for this work was provided by NASA through the NASA Hubble Fellowship Grant No. HST-HF2-51436.001-A awarded by the Space

Telescope Science Institute, which is operated by the Association of Universities for Research in Astronomy, Incorporated, under NASA contract NAS5-26555. We also thank Covestro AG for providing samples of the Bayfol® HX materials. Robert J. Harris is supported by the Deutsche Forschungsgemeinschaft (DFG) through project 326946494, "Novel Astronomical Instrumentation through photonic Reformatting." B. Sinquin is funded by H2020 OPTICON No. 730890. This project has received funding from the European Union's Horizon 2020 research and innovation program under Grant Agreement No. 694513 and No. 730890, from the UK Science and Technology Facilities Council (STFC) – STFC Grant No. ST/N000544/1 and No. ST/N000625/1, from the Bundesministerium für Bildung und Forschung (BMBF), joint project PRIMA (13N14630), the Helmholtz International Research School for Teratronics (HIRST), and the Deutsche Forschungsgemeinschaft (DFG, German Research Foundation) under Germany's Excellence Strategy via the Excellence Cluster 3D Matter Made to Order (EXC2082/1 – 390761711). The authors declare no conflict of interest.

Data, Materials, and Code Availability

All data that were used to support this work can be found at doi: 10.25422/azu.data.12857885.

References

1. I. A. G. Snellen et al., "The orbital motion, absolute mass and high-altitude winds of exoplanet HD209458b," *Nature* **465**, 1049–1051 (2010).
2. D. K. Sing et al., "A continuum from clear to cloudy hot-Jupiter exoplanets without primordial water depletion," *Nature* **529**, 59–62 (2016).
3. L. Kreidberg et al., "Absence of a thick atmosphere on the terrestrial exoplanet LHS 3844b," *Nature* **573**, 87–90 (2019).
4. D. Charbonneau et al., "Detection of thermal emission from an extrasolar planet," *Astrophys. J.* **626**, 523–529 (2005).
5. M. Brogi et al., "The signature of orbital motion from the dayside of the planet τ Boötis b," *Nature* **486**, 502–504 (2012).
6. H. J. Hoeijmakers et al., "Atomic iron and titanium in the atmosphere of the exoplanet KELT-9b," *Nature* **560**, 453–455 (2018).
7. J. L. Beuzit et al., "SPHERE: the exoplanet imager for the very large telescope," *Astron. Astrophys.* **631**, A155 (2019).
8. B. Macintosh et al., "First light of the Gemini planet imager," *Proc. Natl. Acad. Sci. U. S. A.* **111**, 12661–12666 (2014).
9. N. Jovanovic et al., "The Subaru coronagraphic extreme adaptive optics system: enabling high-contrast imaging on solar-system scales," *Publ. Astron. Soc. Pac.* **127**, 890 (2015).
10. A. M. Lagrange et al., "A probable giant planet imaged in the β Pictoris disk. VLT/NaCo deep L'-band imaging," *Astron. Astrophys.* **493**, L21–L25 (2009).
11. M. Bonnefoy et al., "The near-infrared spectral energy distribution of β Pictoris b," *Astron. Astrophys.* **555**, A107 (2013).
12. M. Keppler et al., "Discovery of a planetary-mass companion within the gap of the transition disk around pds 70," *Astron. Astrophys.* **617**, A44 (2018).
13. A. Müller et al., "Orbital and atmospheric characterization of the planet within the gap of the PDS 70 transition disk," *Astron. Astrophys.* **617**, L2 (2018).
14. B. P. Bowler et al., "Planets around low-mass stars (PALMS). IV. The outer architecture of M Dwarf planetary systems," *Astrophys. J. Suppl. Ser.* **216**, 7 (2015).
15. K. Wagner, D. Apai, and K. M. Kratter, "On the mass function, multiplicity, and origins of wide-orbit giant planets," *Astrophys. J.* **877**, 46 (2019).
16. A. Vigan et al., "The SPHERE infrared survey for exoplanets (SHINE). III. The demographics of young giant exoplanets below 300 au with SPHERE," arXiv:2007.06573 (2020).
17. C. Marois et al., "Angular differential imaging: a powerful high-contrast imaging technique," *Astrophys. J.* **641**, 556–564 (2006).

18. J. Antichi et al., "BIGRE: a low cross-talk integral field unit tailored for extrasolar planets imaging spectroscopy," *Astrophys. J.* **695**, 1042–1057 (2009).
19. W. B. Sparks and H. C. Ford, "Imaging spectroscopy for extrasolar planet detection," *Astrophys. J.* **578**, 543–564 (2002).
20. P. Riaud and J. Schneider, "Improving Earth-like planets' detection with an ELT: the differential radial velocity experiment," *Astron. Astrophys.* **469**, 355–361 (2007).
21. H. Kawahara et al., "Spectroscopic coronagraphy for planetary radial velocimetry of exoplanets," *Astrophys. J. Suppl. Ser.* **212**, 27 (2014).
22. I. Snellen et al., "Combining high-dispersion spectroscopy with high contrast imaging: probing rocky planets around our nearest neighbors," *Astron. Astrophys.* **576**, A59 (2015).
23. J. Wang et al., "Observing exoplanets with high dispersion coronagraphy. I. The scientific potential of current and next-generation large ground and space telescopes," *Astron. J.* **153**, 183 (2017).
24. A. D. Rains et al., "Development of the single-mode fiber integral field unit for the RHEA spectrograph," *Proc. SPIE* **10702**, 107025J (2018).
25. S. Y. Haffert et al., "On-sky results of the Leiden EXoplanet Instrument (LEXI)," *Proc. SPIE* **10703**, 1070323 (2018).
26. D. Mawet et al., "Keck planet imager and characterizer: status update," *Proc. SPIE* **10703**, 1070306 (2018).
27. I. A. G. Snellen et al., "Fast spin of the young extrasolar planet β Pictoris b," *Nature* **509**, 63–65 (2014).
28. H. J. Hoeijmakers et al., "Medium-resolution integral-field spectroscopy for high-contrast exoplanet imaging. Molecule maps of the β Pictoris system with SINFONI," *Astron. Astrophys.* **617**, A144 (2018).
29. Q. M. Konopacky et al., "Detection of carbon monoxide and water absorption lines in an exoplanet atmosphere," *Science* **339**, 1398–1401 (2013).
30. T. S. Barman et al., "Simultaneous detection of water, methane, and carbon monoxide in the atmosphere of Exoplanet HR8799b," *Astrophys. J.* **804**, 61 (2015).
31. D. J. M. P. dit de la Roche, H. J. Hoeijmakers, and I. A. G. Snellen, "Molecule mapping of HR8799b using OSIRIS on Keck. Strong detection of water and carbon monoxide, but no methane," *Astron. Astrophys.* **616**, A146 (2018).
32. J.-B. Ruffio et al., "Radial velocity measurements of HR 8799 b and c with medium resolution spectroscopy," *Astron. J* **158**, 200 (2019).
33. K. Wagner et al., "Magellan adaptive optics imaging of PDS 70: measuring the mass accretion rate of a young giant planet within a gapped disk," *Astrophys. J.* **863**, L8 (2018).
34. S. Y. Haffert et al., "Two accreting protoplanets around the young star PDS 70," *Nat. Astron* **3**, 749–754 (2019).
35. S. G. Leon-Saval, C. H. Betters, and J. Bland-Hawthorn, "The photonic tiger: a multicore fiber-fed spectrograph," *Proc. SPIE* **8450**, 84501K (2012).
36. R. J. Harris et al., "Photonic spatial reformatting of stellar light for diffraction-limited spectroscopy," *Mon. Not. R. Astron. Soc.* **450**(1), 428–434 (2015).
37. P.-I. Dietrich et al., "Printed freeform lens arrays on multi-core fibers for highly efficient coupling in astrophotonic systems," *Opt. Express* **25**, 18288 (2017).
38. P. I. Dietrich et al., "*In situ* 3D nanoprinting of free-form coupling elements for hybrid photonic integration," *Nat. Photonics* **12**, 241–247 (2018).
39. R. R. Thomson et al., "Ultrafast laser inscription of a 121-waveguide fan-out for astrophotonics," *Opt. Lett.* **37**, 2331–2333 (2012).
40. A. Boccaletti et al., "SPHERE+: imaging young Jupiters down to the snowline," arXiv:2003.05714 (2020).
41. A. Zanutta et al., "Spectral multiplexing using stacked volume-phase holographic gratings–I," *Mon. Not. R. Astron. Soc.* **469**(2), 2412–2422 (2017).
42. E. Gendron et al., "Final two-stage MOAO on-sky demonstration with canary," *Proc. SPIE* **9909**, 99090C (2016).
43. R. Bacon et al., "3D spectrography at high spatial resolution. I. Concept and realization of the integral field spectrograph TIGER," *Astron. Astrophys. Suppl. Ser.* **113**, 347 (1995).

44. N. Thatte et al., "Very high contrast integral field spectroscopy of AB Doradus C: 9-mag contrast at 0.2 arcsec without a coronagraph using spectral deconvolution," *Mon. Not. R. Astron. Soc.* **378**, 1229–1236 (2007).
45. T. D. Groff et al., "The CHARIS IFS for high contrast imaging at Subaru," *Proc. SPIE* **9605**, 96051C (2015).
46. A. J. Skemer et al., "First light with ALES: a 2-5 micron adaptive optics integral field spectrograph for the LBT," *Proc. SPIE* **9605**, 96051D (2015).
47. A. Vigan et al., "High-contrast imaging of Sirius A with VLT/SPHERE: looking for giant planets down to one astronomical unit," *Mon. Not. R. Astron. Soc.* **454**, 129–143 (2015).
48. J. R. Males and O. Guyon, "Ground-based adaptive optics coronagraphic performance under closed-loop predictive control," *J. Astron. Telesc. Instrum. Syst.* **4**, 019001 (2018).
49. C. Vanderriest, "A fiber-optics dissector for spectroscopy of nebulosities around quasars and similar objects," *Publ. Astron. Soc. Pac.* **92**, 858–862 (1980).
50. J. R. Allington-Smith et al., "Integral field spectroscopy with the gemini multiobject spectrographs," *Proc. SPIE* **2871**, 1295–1305 (1997).
51. D. Mawet et al., "Observing exoplanets with high-dispersion coronagraphy. II. Demonstration of an active single-mode fiber injection unit," *Astrophys. J.* **838**, 92 (2017).
52. E. H. Por and S. Y. Haffert, "The single-mode complex amplitude refinement (SCAR) coronagraph. I. Concept, theory, and design," *Astron. Astrophys.* **635**, A55 (2020).
53. G. Ruane et al., "Efficient spectroscopy of exoplanets at small angular separations with vortex fiber nulling," *Astrophys. J.* **867**, 143 (2018).
54. C. T. Coker et al., "Simulations of a high-contrast single-mode fiber coronagraphic multiobject spectrograph for future space telescopes," *J. Astron. Telesc. Instrum. Syst.* **5**, 045003 (2019).
55. R. G. Petrov et al., "AMBER, the near-infrared spectro-interferometric three-telescope VLTI instrument," *Astron. Astrophys.* **464**, 1–12 (2007).
56. Gravity Collaboration et al., "First light for GRAVITY: phase referencing optical interferometry for the very large telescope interferometer," *Astron. Astrophys.* **602**, A94 (2017).
57. J. R. Crepp et al., "iLocater: a diffraction-limited Doppler spectrometer for the large binocular telescope," *Proc. SPIE* **9908**, 990819 (2016).
58. J. Baudrand and G. A. H. Walker, "Modal noise in high-resolution, fiber-fed spectra: a study and simple cure," *Publ. Astron. Soc. Pac.* **113**, 851–858 (2001).
59. L. S. Fohrmann et al., "Single mode thermal emission," *Opt. Express* **23**, 27672–27682 (2015).
60. J. C. Corbett, "Sampling of the telescope image plane using single- and few-mode fibre arrays," *Opt. Express* **17**, 1885–1901 (2009).
61. N. Jovanovic et al., "Efficient injection from large telescopes into single-mode fibres: enabling the era of ultra-precision astronomy," *Astron. Astrophys.* **604**, A122 (2017).
62. S. Y. Haffert et al., "The single-mode complex amplitude refinement (SCAR) coronagraph. II. Lab verification, and toward the characterization of Proxima b," *Astron. Astrophys.* **635**, A56 (2020).
63. A. D. Rains et al., "Precision single mode fibre integral field spectroscopy with the RHEA spectrograph," *Proc. SPIE* **9908**, 990876 (2016).
64. C. H. Betters et al., "PIMMS Échelle: the next generation of compact diffraction limited spectrographs for arbitrary input beams," *Proc. SPIE* **9147**, 91471I (2014).
65. I. Spaleniak et al., "Integrated photonic building blocks for next-generation astronomical instrumentation II: the multimode to single mode transition," *Opt. Express* **21**, 27197–27208 (2013).
66. D. G. MacLachlan et al., "Efficient photonic reformatting of celestial light for diffraction-limited spectroscopy," *Mon. Not. R. Astron. Soc.* **464**(4), 4950–4957 (2016).
67. C. A. Ross et al., "Optimisation of ultrafast laser assisted etching in fused silica," *Opt. Express* **26**(19), 24343–24356 (2018).
68. N. Jovanovic et al., "Starlight demonstration of the dragonfly instrument: an integrated photonic pupil-remapping interferometer for high-contrast imaging," *Mon. Not. R. Astron. Soc.* **427**(1), 806–815 (2012).

69. T. Gissibl et al., "Refractive index measurements of photo-resists for three-dimensional direct laser writing," *Opt. Mater. Express* **7**, 2293–2298 (2017).
70. Nanoscribe, "Ip photoresins," 2020, https://www.nanoscribe.com/en/solutions/materials#tab-880.
71. A. Zanutta et al., "Photopolymeric films with highly tunable refractive index modulation for high precision diffractive optics," *Opt. Mater. Express* **6**(1), 252–263 (2016).
72. S. Kirkpatrick, C. D. Gelatt, and M. P. Vecchi, "Optimization by simulated annealing," *Science* **220**(4598), 671–680 (1983).
73. S. Noll et al., "An atmospheric radiation model for Cerro Paranal. I. The optical spectral range," *Astron. Astrophys.* **543**, A92 (2012).
74. A. Jones et al., "An advanced scattered moonlight model for Cerro Paranal," *Astron. Astrophys.* **560**, A91 (2013).
75. T. O. Husser et al., "A new extensive library of PHOENIX stellar atmospheres and synthetic spectra," *Astron. Astrophys.* **553**, A6 (2013).
76. R. M. Cutri et al., "VizieR online data catalog: 2MASS all-sky catalog of point sources (Cutri+ 2003)," VizieR Online Data Catalog, II/246 (2003).
77. G. Sivo et al., "First on-sky SCAO validation of full LQG control with vibration mitigation on the CANARY pathfinder," *Opt. Express* **22**(19), 23565–23591 (2014).
78. B. Sinquin et al., "On-sky results for adaptive optics control with data-driven models on low-order modes," *Mon. Not. R. Astron. Soc.* **498**, 3228–3240 (2020).
79. M. Kissler-Patig et al., "HAWK-I: the high-acuity wide-field K-band imager for the ESO very large telescope," *Astron. Astrophys.* **491**, 941–950 (2008).
80. J. R. Males et al., "MagAO-X: project status and first laboratory results," *Proc. SPIE* **10703**, 1070309 (2018).

Sebastiaan Y. Haffert is a NASA Hubble postdoctoral fellow at the University of Arizona's Steward Observatory. He received his PhD in astronomy cum laude from Leiden University in 2019. His research focuses on high-spatial and high-spectral resolution instrumentation for exoplanet characterization.

Robert J. Harris received his PhD from Durham University in 2014, modeling astrophotonic devices and spectrographs and developing photonic reformatters for high-resolution spectroscopy. Following his PhD and a STEP postdoc (again at Durham), he took up a Carl-Zeiss fellowship at the Landessternwarte, Heidelberg, where he was also awarded the Gliese fellowship. He is currently working at the MPIA in Heidelberg.

Biographies of the other authors are not available.